International Journal of High Speed Electronics and Systems
Vol. 25, Nos. 1 & 2 (2016) 1640006 (22 pages)
© World Scientific Publishing Company
DOI: 10.1142/S0129156416400061

World Scientific
www.worldscientific.com

Advances in RRAM Technology: Identifying and Mitigating Roadblocks

D. Veksler

Engineering Physics Division, NIST
Gaithersburg, MD, 20899, USA
dmitry.veksler@nist.gov

G. Bersuker

The Aerospace Corporation
Los Angeles, CA 90009, USA
gennadi.bersuker@aero.org

Received 24 August 2016
Accepted 15 September 2016

Superior scalability, endurance, low power operation, retention, and operating speed of filamentary crystalline HfO_x-based resistive random access memory (RRAM) makes this technology promising for implementation in exascale neuromorphic computing systems. Challenges, roadblocks for the implementation, and possible resolutions are discussed. Technological solutions to overcome RRAM variability issues (both device-to-device and cycle-to-cycle) and read instability are evoked. Comprehensive understanding of basic physics mechanisms of RRAM operation allows identification of major material properties and operation conditions controlling performance of the crystalline HfO_x-based RRAM.

Keywords: RRAM technology; RRAM reliability; RRAM variability; RRAM read instability; RTN in RRAM; HfO_2; neuromorphic computing systems

1. Introduction

The Resistive Random Access Memory (RRAM) concept in non-volatile memory technology[1-6] is based on controllably varying conduction through the isolating layer. In filament-based RRAM technology, which is advantageous due to device scalability, high speed, and low power operations, a current through the dielectric film is determined by a conductive filament formed through the insulating media. This filament (as well as multiple non-filament conductive paths preferentially formed in some materials) can be repeatedly ruptured and restored by applying voltage that define higher and lower resistance states, each of which corresponds to a certain cell memory state.[3] RRAM technology promises to deliver a “universal memory” device which could cover memory requirements for different applications ranging from storage to embedded memories, i.e., static random-access memory (SRAM), flash memory, and dynamic random-access memory (DRAM) technologies (Table 1) as follows from the demonstrated endurance,[7] retention,[8] and speed.[9-11]

Resistive switching was demonstrated in a number of dielectric materials (binary oxides: TiO_2, HfO_2, SiO_2, Ta_2O_5, Al_2O_3, etc.; ternary oxides: $BaTiO_3$, etc.; nitrides: hexagonal Boron Nitride, etc., and even organic materials[12]) sandwiched between metal electrodes and forming a metal-insulator-metal (MIM) capacitor. Although commercial RRAM products have become available,[13,14] there is not yet a clear path for implementation of RRAM technology in a wider variety of memory products. In particular, significant research efforts are required to overcome variability and instability issues inherent to RRAM devices in order to utilize the entire range of technology advantages. The existing models of RRAM operation, ranging from phenomenological and semi-empirical[15-17] to Monte Carlo and molecular diffusion based approaches,[18-21] vary on the physical processes responsible for resistive switching, leaving uncertain the ways of controlling device characteristics. RRAM operation is driven by diffusion of oxygen ions and vacancies,[3,18,21] requiring higher activation energies[3] that generally may lead to higher operation voltages and variability, and make it more challenging to scale the filament dimensions. On the other hand, a higher threshold for activating structural changes associated with the rearrangement of oxygen atoms in the memory cell leads to outstanding retention of memory states and stability against various environmental conditions, e.g., temperature, radiation exposure, etc.[22,23] It was recently shown[24] that, under the optimized ultra-fast pulsed forming and switching operations, polycrystalline HfO_2-based RRAM offers excellent control over variability and retention of the resistive states and is promising for low bit error rate operations. Alternative promising nonvolatile memory (NVM) techniques include Conductive Bridge RAM (CBRAM) where conductivity is modulated by metal ions (Cu, Ag, etc.) diffusing in/out of an isolating layer. CBRAM may be beneficial for low energy operation, since the metal ions forming conductive paths may have relatively low diffusion activation energies; this technology was shown to exhibit fast switching operations, lower variability, and good scalability.[25,26]

RRAM cells are considered for use in neuromorphic computing circuitry (NCC)[27-30] where they are expected to provide further gain in energy efficiency by replacing complex circuitry that mimic biological synapses. Electronic synapses based on RRAM technology are extremely scalable (down to the size of the filament) and can switch between multiple memory states to realize adaptive algorithms for machine learning, pattern recognition, etc. The requirement of precise control of the RRAM states makes the device-to-device reproducibility of device parameters, device cycling, and read stability a challenging and important metric. The state-of-the-art demonstrations of memristive neuromorphic networks so far have required the access to individual cells in a memory array that limits the practically achievable network density.[30]

Meeting variability and stability metrics requires one to establish the mechanism governing charge carrier' interaction with the material structural features. In this framework, the device parameters of the entire set of electrical measurements should be analyzed and related to the atomic-level material structure. Below, we focus on addressing the cell stability based on an understanding of the RRAM switching mechanisms, and identify issues and possible paths for their resolution.

Table 1. Comparison of key characteristics of different memory technologies.

	SRAM	**DRAM**	**Flash NAND**	**Flash NOR**	**RRAM**
Non-volatile	No	No	Yes	Yes	Yes
Cell size (F^2)	≈ 50	≈ 6	≈ 6	≈ 10	≈ 4
Multi-Level-Cell (MLC)	No	No	Yes	Yes	Yes
Write/Erase time	1 ns to 100 ns	50 ns / 50 ns	1 µs / 0.1 µs	1 µs / 10 µs	< 1 ns
Endurance (number of Write/Erase cycles before failure)	10^{16}	10^{16}	10^{5}	10^{5}	$> 10^{13}$
Write current	low	low	very high	very high	low (< 10 mA)
Voltage required	1 V	1.35 V to 1.5 V	3.3 V to 5 V	1.7 to 3.6 V	< 1.5 V
Complexity of 3d integration	high	high	high	high	low

2. Physics of RRAM Operation and Modelling Approach

RRAM operations are based on the formation of a conductive path (filament) through the isolating layer, and its subsequent repeatable partial disruption and recovery. Forming the conductive filament in metal oxides involves creation of a metal-rich region that requires (a) breaking metal-oxygen bonds followed by (b) out-diffusion of released oxygen ions. Both processes, bond breakage and oxygen diffusion, are associated with overcoming certain energy barriers. Under an applied voltage, continuing oxygen vacancy generation leads to higher electron flow (higher current), which further increases the vacancy generation rate, reaching the fast runaway phase of oxygen ion expulsion and formation of a conductive path (dielectric breakdown). Limiting the maximum current through the dielectric, for instance, by connecting a cell in-series to a current-limiting device, allows one to limit the local temperature along the current path and, consequently, the size of the forming filament (Fig. 1). In order to change the cell resistance to a high value (that is, to

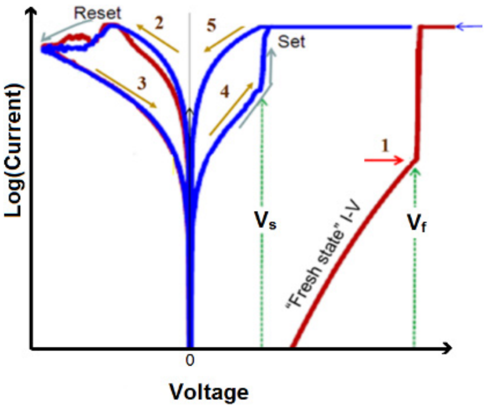

Fig. 1. Current-voltage characteristics of RRAM cell operations: forming – formation of a conductive filament (1), reset – partial disruption of the filament (2,3), and set – filament restoration (4,5).

reset the memory state), the filament should be partially disrupted. This is achieved by applying an opposite bias (in the case of bi-polar switching cells) to the electrodes, again increasing the Joule heating in the vicinity of the filament that leads to re-oxidation of a section of the filament. Switching back to the low resistive state (to SET the memory state) is achieved by applying an initial bias polarity. This time, restoring a small disrupted section of the filament requires smaller energy and, consequently, takes place under significantly lower voltages compared to that of the forming process. The process of setting/resetting (switching) needs to be stable and reproducible for a number of switching cycles as required by the application.

Since forming and set/reset operations are controlled by an atomic restructuring of the dielectric material under external perturbations (voltage, temperature, etc.) they are essentially random processes that result in variability of the filament properties with switching cycles. Based on our understanding of the switching mechanism, variability can be addressed by optimizing operating conditions, reducing parasitics, and by employing certain types of program-verify techniques. Among the considered RRAM materials, HfO_2 is one of the most promising. HfO_2 is an extensively studied fab-friendly material, which had been introduced as a high-k gate dielectric into the mainstream CMOS manufacturing. Electrical characteristics of poly-crystalline HfO_2 films are strongly influenced by their multi-grain structure, specifically grain boundaries (GB), Fig. 2. Modeling studies[31,32] reveal that GBs can accumulate positively charged oxygen vacancies. Released positively charged oxygen ions move interstitially (over the barrier of approximately 0.6 to 0.7 eV) across the grains. Grain boundaries provide an effective electrical current path driven by the trap assisted tunneling via oxygen vacancies,[33] which tend to accumulate there.

Conductive atomic force microscopy (C-AFM) studies[34] revealed that GB oxygen deficient regions form preferential conductive paths serving as precursors of the conductive filament (Fig. 3).

Electron hopping between vacancies along GB increases the temperature around the path promoting generation of additional vacancies[33] and, hence, higher current. In a runaway stage of the filament formation (Fig 2c), oxygen vacancies generated in close

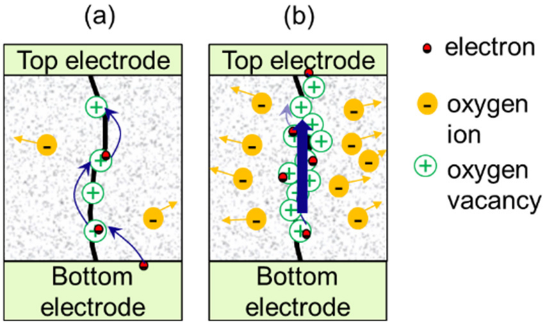

Fig. 2. Schematics of the filament formation process.[31,32] (a) Electrons hopping via positively charged oxygen vacancies along the grain boundary assists releasing oxygen ions and generating new vacancies. (b) Current increase induces a run-away process of the oxygen vacancy/ion pairs generation.

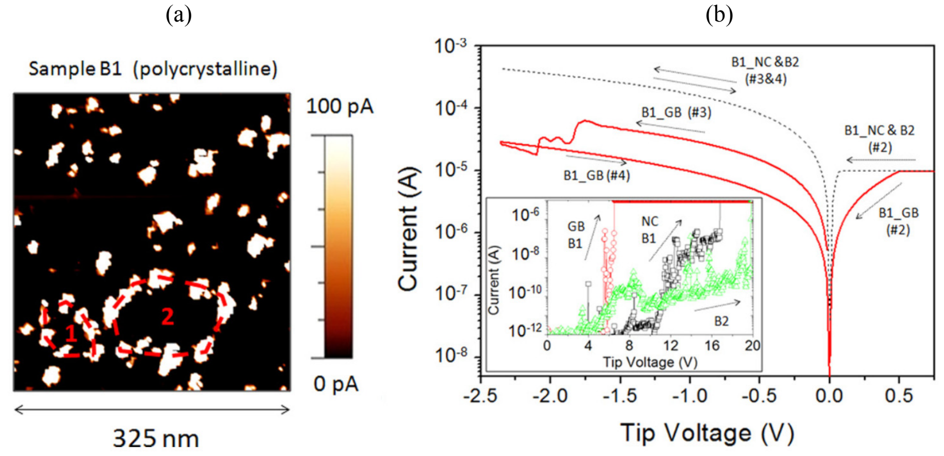

Fig. 3. (a) Conductive AFM current maps as measured above the current noise level at a low voltage. A granular structure is observed since GBs are more conductive than grains. (b) Typical I-V curves collected after the forming (see inset). Samples B1 and B2 contain crystalline and amorphous HfO_2, respectively. GB, NC, refer to grain boundary and grain sites; (#) indicates ramp number. Resistive switching was observed only when tests were performed at the GBs of polycrystalline stacks (exhibiting low-V_{BD} during the forming). After Ref. 34.

proximity form Hf-rich clusters expressing metallic transport characteristics. With further current increase through the filament, the local temperature may reach extremely high values (≈ 800 °C to 1000 °C).[3] Singularities of the electric field at the rather abrupt Hf-rich clusters' interface with the adjoined dielectric material elevates the probability of the interfacial Hf-O bond breaking and releasing oxygen ions into the vicinity of a GB. Such oxygen ion generation and diffusion assisted by temperature and the electric field, leads to the filament growth until the current reaches a curtain predefined magnitude (the compliance current). Subsequently, when the voltage across the cell drops, the current increase stops and leads to disruption of further filament growth. During the post-forming (relaxation) phase some oxygen ions, which remained in the vicinity of the filament, may recombine with the oxygen vacancies there resulting in partial re-oxidation of the formed filament. To form a stable filament of a targeted resistivity, it is therefore important to maintain a balance between the rates of oxygen ions generation and their diffusion away from the forming filament for the duration of this process. In particular, forming at a higher applied voltage may generate densely packed vacancies (filament) much faster than the released oxygen ions can diffuse through the surrounding dielectric region. A significant number of the close-by ions at the end of the filament forming process enables filament re-oxidation, greatly increasing its resistance. In the case of bi-polar RRAM devices, a memory state is changed by applying a bias of opposite polarity. Then, oxygen is forced to move back toward the positively biased electrode where they accumulate and may get injected into the adjacent filament tip and recombine with the vacancies, thus re-creating an oxide layer. This layer constitutes a tunneling barrier for electron transport and resets the filament resistance to the high resistance state. SET is similar to forming although it is a self-limited breakdown process. The above described mechanism of oxygen generation and diffusion is stochastic in nature and makes the structure of a metallic filament slightly different after each set/reset cycle. Such differences, if significant, may add to device parameter variability and sometimes instability (in particular, due to incomplete switching). Mitigating these factors requires optimizing the cell materials and operation conditions.

Grain boundaries stretched along the grains surrounding the filament in the memory cell play an important role in memory switching processes: positively charged oxygen vacancies in GBs attract oxygen ions (negatively charged), released from the filament region, thus restricting their diffusion further away from the filament during set operations. In the case of unrestricted lateral diffusion, a significant amount of oxygen ions generated during set would diffuse far away and not be able to return to the filament to provide a sufficient supply of ions for re-oxidation of the oxide barrier layer. Loss of the oxygen ion supply proceeds with each switching cycle and gradually reduces the filament resistance until it permanently sticks in a low resistance state. Preventing runaway of oxygen ions to GBs neighboring the filament preserves the oxygen supply required for an extensive sequence of set/reset cycles ensuring stable operation and endurance.

The model discussed above for HfO_2 RRAM operations[35] is described by molecular diffusion simulations[21] accounting for the probability of generation of oxygen ion/oxygen vacancy pairs and ion diffusion employing Monte Carlo approach. It calculates Joule heat dissipation in each unit volume of a cell (in simulations, a unit volume size was selected to match the lattice constant of HfO_2), and numerically solves Fourier heat-transfer and charge continuity equations to determine the temperature and electric field values in each unit volume. Then, the number of oxygen vacancies in each unit volume is calculated and the conductivity of this oxide unit is assigned a certain value based on its stoichiometry (Fig. 4).

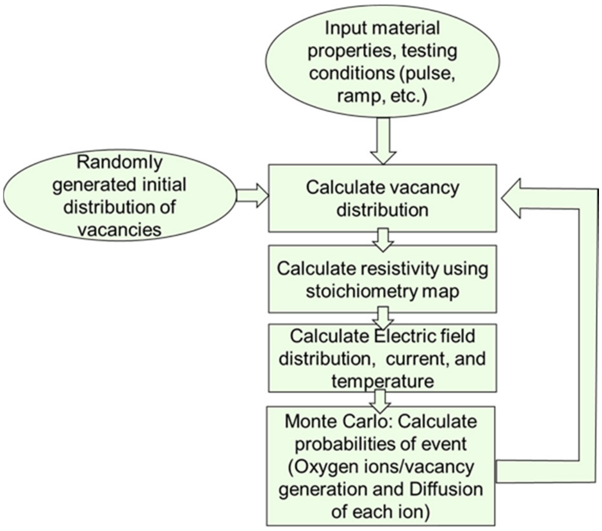

Fig. 4. Flow chart of the molecular diffusion simulations approach used to analyze the dynamics of the conductive filament operations. After Ref. 21.

3. Variability from the Modeling Standpoint

The above described model is applied to address: optimization of composition/operation conditions, filament engineering for low power and high speed, uniformity control due to randomness of the forming process, noise and variability reduction.

As demonstrated by the simulations, Fig. 5, the model links the dielectric grain structure, in particular, the spatial distribution of GBs around a conductive filament (formed along one of the GBs) and density of oxygen vacancies along these GBs, to a distribution/density of oxygen ions released from the filament forming. The model reveals the dependency of device switching properties on oxide stoichiometry and density of the pre-existing oxygen vacancies, capturing the effects of oxygen ion generation and diffusion. Taking the model to the next level by including the recombination of oxygen and oxygen vacancies, we address the scaling challenge, which is reflected in the increasing instability of the filament with the reduction of its size and operating current. The model reproduces the experimental distributions of the filament resistance in the case of different switching conditions (Fig. 6).

As follows from the distribution of filament resistances after forming at a constant voltage stress, device-to-device variability lowers with lower forming voltages (at each current compliance level). These results can be understood through the balance between generation, diffusion, and recombination of oxygen ion/vacancy pairs. Under higher electric field the vacancy generation proceeds faster, increasing its time gap with the process of oxygen out-diffusion (removal) from the vicinity of the filament. Consequently, oxygen ions more efficiently recombine with the vacancies during the following relaxation

(a) No pre-existing vacancies → Strong oxygen out diffusion

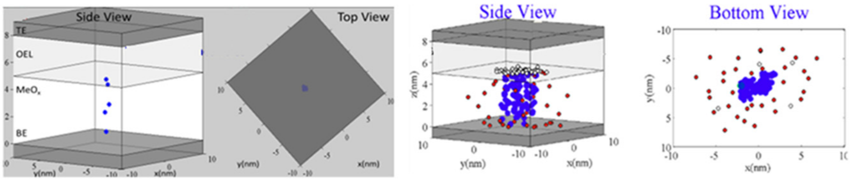

(b) Medium O(+) density → Optimum O- ions generation/retention

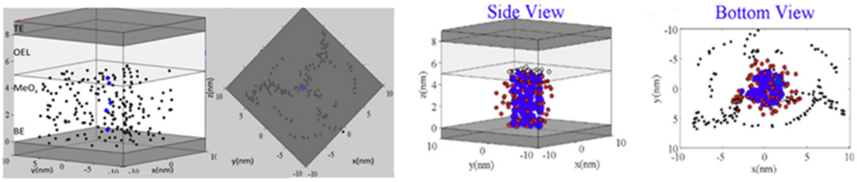

Fig. 5. The role of grain boundaries in retaining released oxygen ions in the filament vicinity. Black circles: oxygen vacancies distributed along GBs; blue circles designate oxygen vacancies composing the filament. Red circles: oxygen ions. (a) An example of a cell having a single GB: oxygen ions released during the filament formation process diffuse away from the filament and may not be able to deoxidize it during a re-set operation. (b) An example of a cell consisting of 3 grains. Positively charged vacancies along the GBs pin diffusing oxygen ions maintaining their presence in the filament vicinity. After Ref. 21.

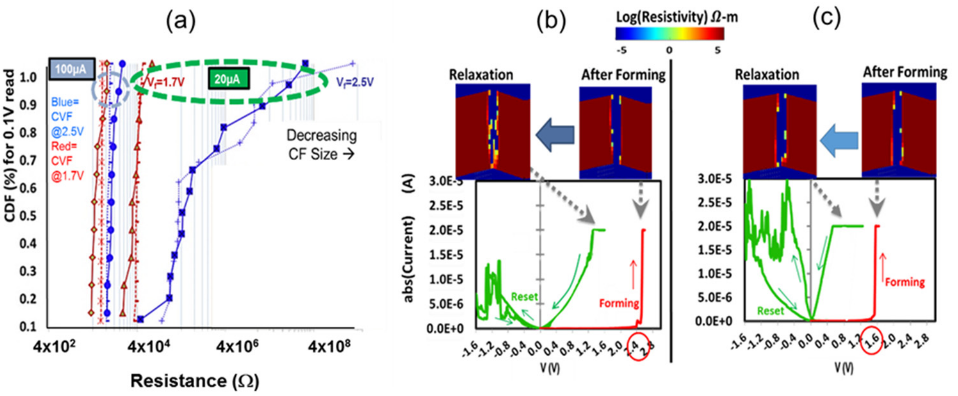

Fig. 6. (a) Experimental (solid curves) vs. theoretical (dotted curves) distributions of filament resistances for different forming voltages. (b,c) Simulations of the 2d resistivity distributions in the cross-section along the conductive filament after high-voltage (b) and low-voltage (c) forming. Simulated resistivity distribution plots show post-forming relaxation in both cases. The corresponding measured device forming and switching I-V characteristics reveal higher filament post-relaxation resistivity (non-Ohmic) (b) and inability to switch to a higher resistance state (to reset) under higher voltage forming due to oxygen out-diffusion. After Ref. 21.

stage, when the bias is removed while the local temperature remains high for an extended period of time. Thus, in the case of higher voltage forming, the filaments are more sensitive to the post-forming random distribution of surrounding ions resulting in greater device to device variability.

4. Effect of Parasitics

Another possible cause of variability is parasitics. The resistance of a RRAM cell during forming under voltage stress (ramping as well as constant) changes by several orders of magnitude within an extremely short time (< 1 ns). When the targeted current value is reached, the current compliance limiting device (e.g., a transistor in series with the cell) prevents further current increase and associated conductive path (filament) growth. However, even in the case of the ideal current limiting device, parasitic capacitance, which might be present in connected circuitry, discharges through the newly formed conductive filament (a so-called current overshoot) lead to further increase of the filament size. This parasitic capacitance can include the capacitance of the cell itself, cables, strip-lanes, contacts, etc. between the compliance limiter and the RRAM cell. In the example shown in Fig. 7, the forming is performed in (1T1R – transistor in series with RRAM cell) and (1R – without a transistor in series) configurations: the overshoot in the 1R case is reflected in the peak reset current being significantly larger than the targeted/recorded compliance current. This data demonstrates that in the case of monolithic integration of the RRAM cell and transistor, which plays the role of a current compliance limiter, the parasitic effect can be negligibly small, with no overshoot observed.

Precise control over the total switching energy may not only eliminate the overshoot, but also reduce variability and improve device-to-device and cycle-to-cycle uniformity.[36]

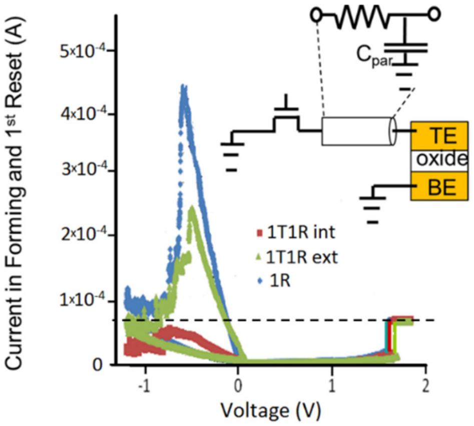

Fig. 7. (a) Switching I-V characteristics measured using slow (≈ 1V/s) voltage sweep in a monolithic 1T1R device (with minimum parasitic capacitance) – red curve; 1T1R with the external transistor situated outside of the tested wafer area (green curve); and without transistor in series with the 1R RRAM cell, utilizing compliance of SMU. The inset shows schematic of the equivalent circuit with the parasitic capacitance responsible for overshoot.

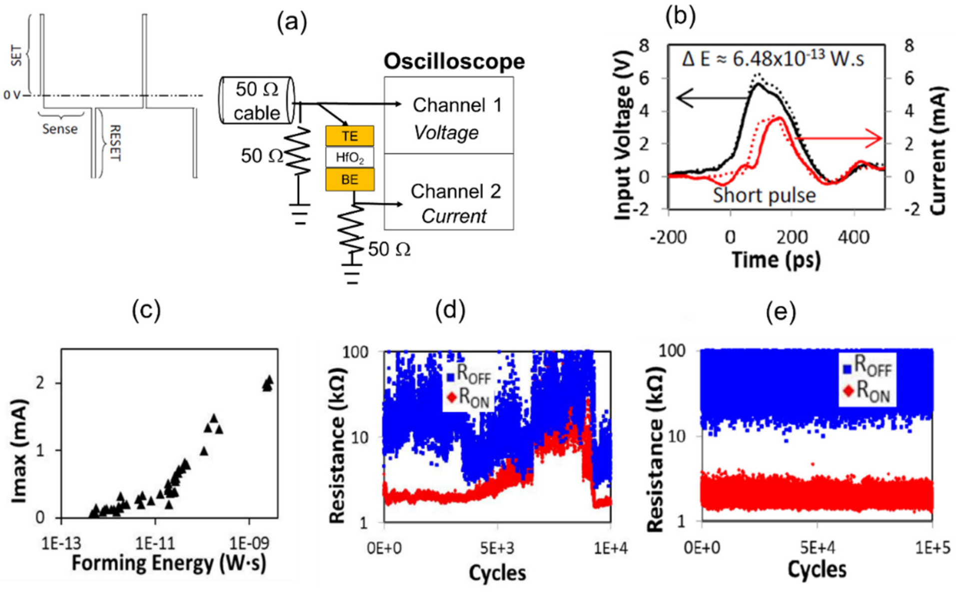

Fig. 8. (a) Schematic of the experimental set up and applied pulse sequence. Note the absence of compliance device. All connections are consistent with proper high speed signal integrity. 50 Ω termination at the probe provides a fast path to dissipate the charges stored by the parasitic elements, effectively eliminating any overshoot. (b) Voltage and current pulse waveforms (current pulse waveform is extracted via removing the displacement current contribution) utilized to form RRAM devices. (c) Dependence of the maximum current measured through the filament during forming vs. forming energy. (d) Example of failure of the endurance test when filament is formed with too low energy. (e) Excellent endurance through 10^5 set/reset cycles. After Ref. 9.

Control over forming and switching energy was shown to be effectively implemented by applying ultrashort voltage pulses (in ≈ 100 ps to a few ns range).[9,24] The cell resistance is checked after each pulse, and the pulses are repeated until the desired resistance of the cell is reached. This approach does not require implementing current compliance and is overshoot free, because the energy delivered by each pulse is determined by its amplitude and duration and can be programmed to be as small as desired (Fig. 8). This compliance-free approach proved to provide more stable switching compared to DC and conventional microsecond pulse operation.

The compliance-free switching approach is especially promising for neuromorphic applications due to improved operation stability and the absence of compliance limiting devices. Transistor-based compliance devices have a significantly larger footprint than the RRAM cells and limits the volume cells density needed in the future exascale neuromorphic computing systems.

5. Cycle to Cycle Variability

As discussed above, RRAM devices demonstrate attractive operation capabilities of practical importance such as high speed: switching of small filaments requires limited atomic movements; low energy: atomic rearrangements require small activation energy and occur in extremely limited dielectric volume; ultra-scaling: RRAM cell area size is limited by grains dimension (≈ 10 nm); excellent retention: high barrier for spontaneous Hf-O bond breakage; manufacturability: fab-friendly materials are used to build the RRAM cell; 3D integration: multi-layers vertical integration is demonstrated.[37] However, there are serious challenges: filament forming and switching are associated with bond breakage and ions diffusion processes, which are probabilistic in nature and, therefore, the resulting filament structure and its electrical characteristics may vary (cell-to-cell, cycle-to-cycle) depending on the employed conditions – thus, a certain degree of variability is expected (Fig. 9). In general, each set/reset cycle may result in the filaments having somewhat different atomic structures.

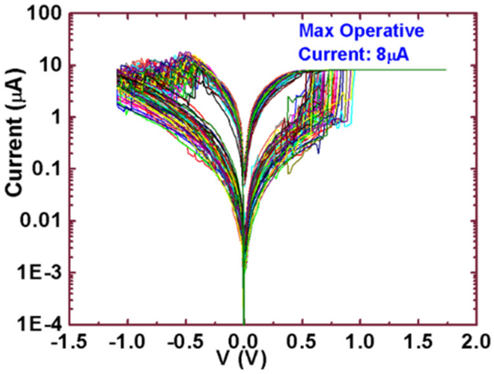

Fig. 9. Switching current-voltage characteristics measured in 50 consecutive set/reset cycles in HfO_2 RRAM cell. x2 to x5 variation of state currents is observed because of the filament variability from cycle-to-cycle.

Cycle-to-cycle variability was evaluated using the developed automated measurement procedure[36] where the sequence of the SET / RESET and read voltage pulses was applied to the RRAM device and the corresponding currents were measured (Fig. 10). The SET and RESET pulses had the rise/fall time of 10 μs and pulse width of 1 μs. The SET and RESET pulse amplitudes were 2 V and -1.5 V, respectively.

Excluding the lower current tail observed in ≈ 6 % cycles, the low resistive state (LRS) current exhibits a normal distribution, which can be characterized by the mean (μ_{LRS}) and standard deviation (σ_{LRS}) parameters. The linear *I–V* dependency (see insert in Fig. 11) points to the filament ohmic characteristics and, hence, the current values are expected to change linearly with the filament cross-section and resistivity, variations of which explain

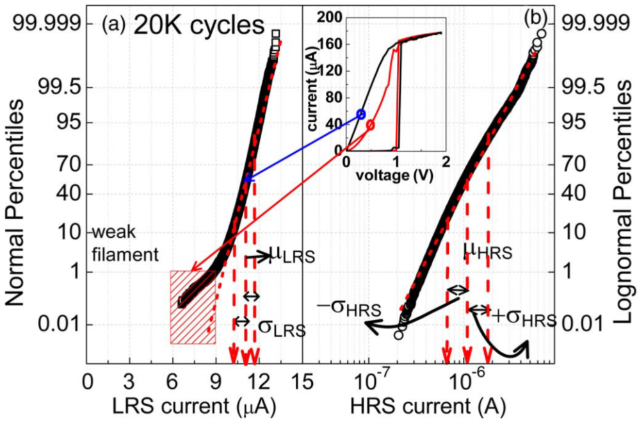

Fig. 10. Schematic of the experimental set up for fast RRAM cycling. Right panel shows voltage and current waveforms obtained in the experiment. Programing pulses are followed by low voltage 0.1 V read pulses. LRS and HRS are low (L) and high (H) resistive states, respectively. After Ref. 36.

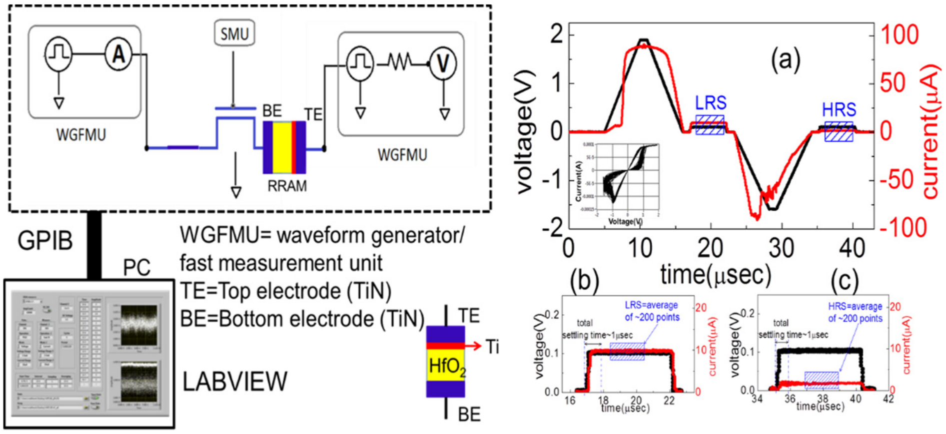

Fig. 11. (a) LRS current and (b) HRS current distribution in a device subjected to 20000 set/reset cycles. Inset shows the I-V characteristics of set transition in case of normal complete switching (black) and abnormal incomplete switching (red curve). After Ref. 36.

the origin of the LRS (low resistance state) normal distribution. The lower current tail is related to the incomplete breakdown of the dielectric barrier layer formed in the filament by the reset operations (driving cell transition to HRS, high resistance state) as follows from the non-ohmic *I*–*V* characteristics (the inset in Fig. 11).

Unlike LRS currents, the HRS currents follow a lognormal distribution, and, therefore, its variability can be described by the mean (μ_{HRS}) and standard deviation (σ_{HRS}) of this logarithm dependency. The HRS currents exhibit a non-linear *I*–*V* dependency as it is governed by the trap assisted tunneling (TAT) conductance through the oxide barrier layer in the filament.[3] The variation in the HRS current is caused by the variation in the distribution of defects (oxygen vacancies) in the oxide barrier layer that dominate the electron transport through the barrier.[38] The log-normal distribution of the HRS current is a consequence of the exponential dependency of the current magnitude on the defect density. Note the difference in the dependencies of mean HRS and LRS resistances on the pulse duration (opposite) (Fig. 12).

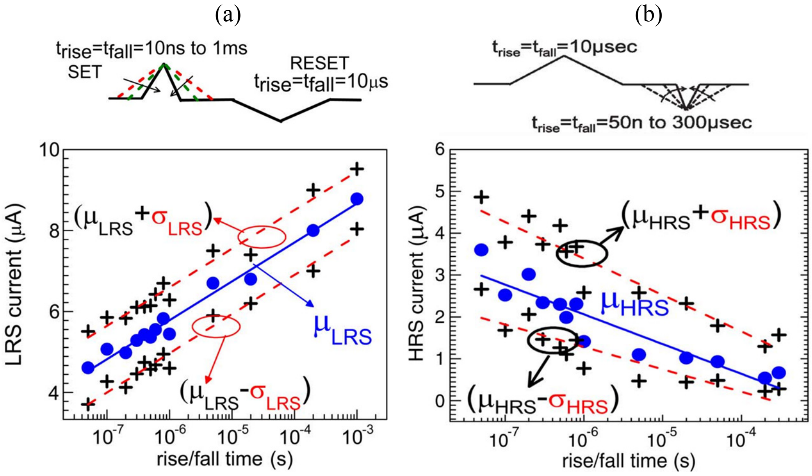

Fig. 12. Dependence of extracted parameters of (a) LRS and (b) HRS currents distributions. μ_{LRS} and $\mu_{\mathrm{LRS}} \pm \sigma_{\mathrm{LRS}}$; μ_{HRS} and $\mu_{\mathrm{HRS}} \pm \sigma_{\mathrm{HRS}}$ for different set/reset pulse conditions (shown in top panels of the figure). After Ref. 36.

LRS current reduces linearly with the exponential reduction of the set pulse time while σ_{LRS} remains approximately constant. With shorter set t_{rise} and t_{fall} times, some generated oxygen ions may not have sufficient time to out-diffuse, which may lead to their back-recombination with the formed vacancies, and, hence, higher filament resistivity and lower LRS current. In this case, σ_{LRS} can be expected to remain constant since the underlying stochastic processes of the oxygen ion movement, controlled by temperature, electric field and intrinsic structural properties of the dielectric, are not expected to depend strongly on the filament radius.

In RESET, both μ_{HRS} and $\pm\sigma_{\mathrm{HRS}}$ increase with the reduction in the pulse rise/fall times. This can be understood considering that the applied bias and oxygen ions concentration gradient drive ions back to the filament leading to its partial oxidation (leading to the oxide barrier formation). A shorter reset pulse time limits the number of oxygen ions diffusing to the filament leading to a thinner barrier and, hence, higher HRS current. Consistent with this explanation, larger $\pm\square_{\mathrm{HRS}}$ is observed for shorter reset pulses due to a larger number of the defect sites in the formed dielectric barrier. Consequently, faster switching RRAM operations (shorter switching times) should lead to lower LRS and higher HRS currents, thus closing the memory window.

More promising results were obtained with the compliance-free switching approach[9,24] when extremely short (100 ps) repeated voltage pulses are applied to the RRAM device until the targeted resistance is reached. The processes of oxygen generation and diffusion in this case are activated only for the very short times, while high electric field is present in the vicinity of the filament and the local temperature is still high enough. This approach is shown to result in consistent switching of each set/reset cycle, with excellent endurance and repeatability.[24] Accurate evaluation of the physics behind switching in the compliance-less mode requires further modeling and investigation.

6. Statistics of Read Instability in RRAM

The exceptional scalability of RRAM devices is driven by a filamentary formation/switching process utilizing GB features of the dielectric material. However, scaled down filament cross-sections and reduced operating currents cause increased variability of the HRS and LRS resistances. In the previous section, we discussed variations of the RRAM resistances from one write/erase (set/reset) cycle to another. This variability is caused by the random generation/annihilation of oxygen vacancies during switching, and the fact that the distribution of these oxygen vacancies constituting a filament is different from cycle-to-cycle. More variability of state resistance is caused by the instability of a RRAM state resistance after the switching event already took place. It is possible to identify two possible causes of this instability: (a) irreversible random structural changes of the filament that involves the creation/elimination of atomic defects contributing to the current transport located in the filament itself or in the surrounding oxide in the vicinity of the filament (there is a non-zero probability of these changes while monitoring the state resistance using low read voltage, which is orders of magnitude lower than the switching voltage); (b) by a repeatable capture/emission of electrons by a defect created during switching. These fluctuations typically switch the RRAM current between several distinct levels, similar to that of Random Telegraph Noise (RTN) phenomena observed in MOSFET drive current.[39] The amplitude and number of levels of the current fluctuations depends on the applied voltage (Fig. 13) and changes from cycle to cycle. This instability effectively reduces the memory window and thus limits scaling of operational currents/filament sizes.

Historically, RTN in MOSFETs has been attributed to changes of the drain or gate currents caused by random charging/discharging of defects in the gate oxide of a transistor.[40] In significantly small devices, when charge carriers in the channel can interact with only a few defects in the oxide, analysis of RTN yields characteristic capture and emission times of the said defects, and is useful for isolation of the processing issues and for gate stack optimization. Consideration of RTN phenomenon in RRAM should be very

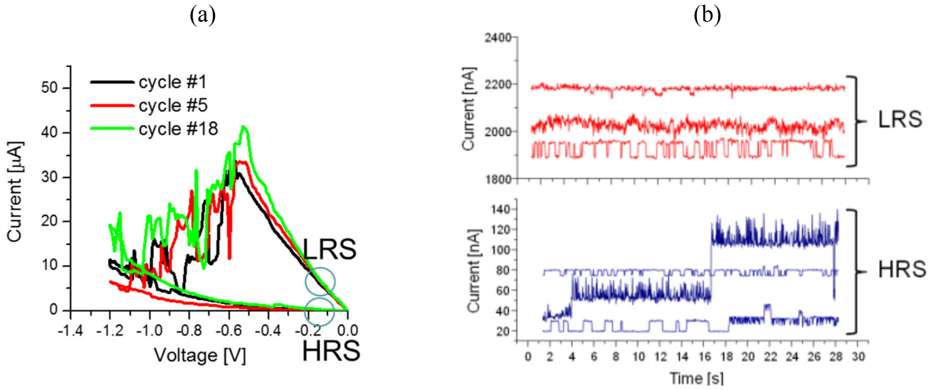

Fig. 13. (a) Typical reset I-V curves out of several set/reset cycles. (b) T=300 K, tread=30s. (b) The corresponding read current traces in HRS and LRS in these set/reset cycles. Device: 1 x 1 μm^2 TiN/5 nm HfO$_2$/TiN. After Ref. 44.

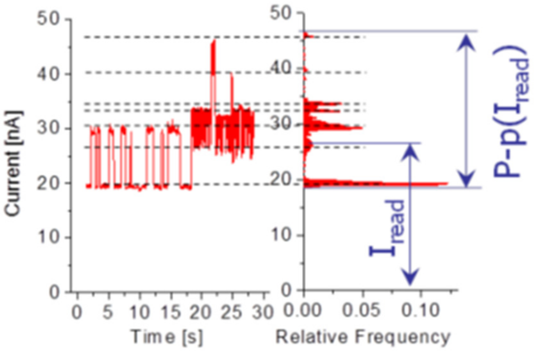

Fig. 14. The read current vs. time and corresponding histogram of the read current values. Peaks in the histogram correspond to the RTN levels observed during the actual (limited) measurement time. Iread represents the mean DC current of the corresponding resistive state. P-p(Iread) is the FoM of read instability and is directly related to the amplitudes of the RTN signals. After Ref. 44.

different. Physically, the electron transport along the filament, in both HRS and LRS, is modulated by the local electric field formed across the current path when a nearby defect site traps an injected electron. Such sites, in particular oxygen vacancies, which are getting created/annihilated during switching cycles, can trap and release electrons causing fluctuations of electric field in the filament. Consequently, the observed RTN instability varies significantly from cycle-to-cycle, driven by randomly generated defects. Therefore, analysis of individual RTN signals[41,42] does not yield sufficient information. A quantitative approach for the description of the effect of RTN-induced reading instability was implemented.[43,44] This approach analyzes read instability amplitudes in a statistically significant number of cycles of individual RRAM cells, and allows projecting it to arrays of cells. The maximum variation of a read current, called Peak-to-peak (P-p) amplitude, was proposed as a figure of merit (FOM) for the read instability (Fig. 14). This maximum variation is associated with the event when all possible random changes producing the current fluctuation occur simultaneously, which constitutes the worst-case scenario for the erroneous read of the memory state. This FOM allows evaluating instability over a number of cycles to obtain statistics and predict the maximum expected error for the given operating conditions, filament cross-section, and to analyze the physical processes responsible for the observed current fluctuations.

To separate the effect of possible structural changes occurring during the period the cell remains in a given state (in between switching events) from the effect of pre-existing defects formed by the switching process, read instability was measured under a wide range of applied voltages. It was observed that P-p fluctuations scale proportionally to I_{read}, which implies that its increase with V_{read} is caused by higher current density while the current path does not change. The structural changes of the current path would cause an irreversible change of the current density. Structural changes are more likely to occur at higher read voltages, those reduce the activation energies for defect creation. A linear correlation between the mean read current averaged over 200 set/reset cycles, and averaged P-p variations of the read current is observed for both high and low resistance states, Fig. 15. Fig. 15 (b) shows an example of the P-p metric dependency on the mean read current value collected in a set/reset cycle in which the structural changes of the filament occurred. Current fluctuations dropped dramatically at higher read voltages indicating change in the current density, i.e., change in the filament cross-section. The measurements of P-p and Iread in a wide range of read voltages, V_{read} = 10 mV to 200 mV, have demonstrated that the structural changes occurred only in a limited number of cycles, and the read instability in the considered voltage range is determined primarily by defects created during switching.[43,44]

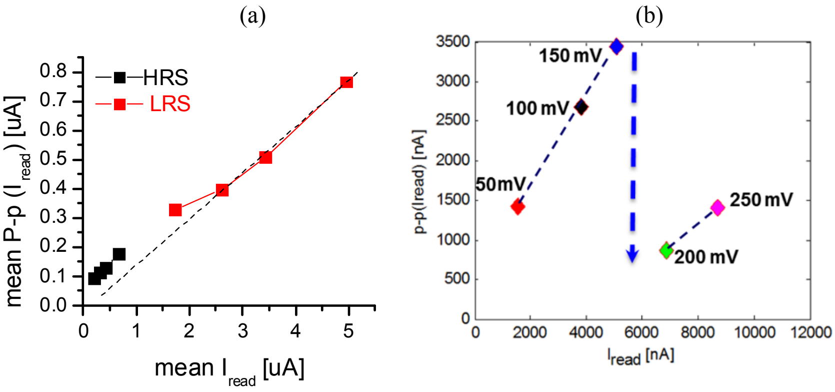

Fig. 15. (a) Peak-to-peak variation of the state read current averaged over 200 set/reset cycles vs. mean read current, averaged over the same 200 cycles. Linear correlation of variation amplitude and mean read current is observed for both high and low resistance states. (b) Example of dependence of P-p metric versus the mean read current as the read voltage increases in a rare cycle in which the structural changes of the filament happened between programming attempts. LRS and HRS resistances are monitored for 30 s after each set or reset. After Ref. 44.

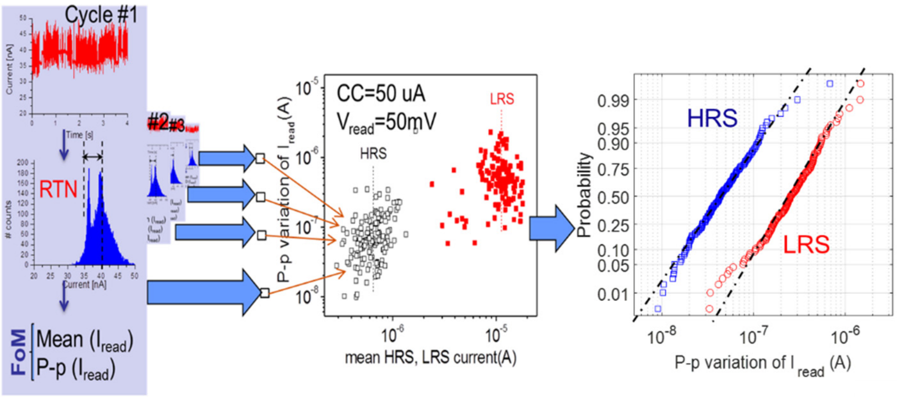

Fig. 16. Mean read currents and peak to peak current fluctuations amplitudes are extracted from measured current waveforms in each set/reset cycle. Right panel shows c.d.f. of peak-to-peak fluctuation amplitudes distribution over 200 set/reset cycles, presented using normal probability plot technique (using special coordinate system in which normal distribution is represented by a single straight line). Distributions of peak-to-peak fluctuation amplitudes over a number of cycles was found to follow the Log-Normal distribution in both LRS and HRS.

As mentioned above, in each reset/set cycle the filament has a slightly different local structure and, consequently, different *mean*(I_{read}) and *P-p*(I_{read}) values. Measuring the distribution of mean read currents (*mean*(I_{read})) and P-p fluctuations over the large number of cycles allows one to obtain a statistical distribution of the fluctuation amplitudes and to assess the effect of these fluctuations on the device performance and reliability. P-p amplitudes are shown to follow a log-normal distribution (Fig. 16), whose parameters depend on the operating conditions. Scaling down the filament width while reducing the operation currents reduces the average fluctuation amplitude. Average read currents, $\mathrm{I_{HRS}}$ and I_{LRS} at the same read voltage of 50 mV are naturally smaller with a narrower filament. The average P-p fluctuation amplitude (amplitude of read instability, while reading the state current in each set/reset cycle) and its dispersion values are obtained by fitting P-p data collected over a large number of cycles on a given device to a log-normal distribution, Fig. 16. These parameters define the entire distribution in both high and low resistance states. For successful operation of RRAM devices, the requirement is for the fluctuation amplitude to be less than the memory window. The average fluctuation amplitude was found to decrease with the reduction of the compliance current (resulting in a smaller filament width) proportionally along with the memory window (Fig. 18, 19). This fact is favorable for scaling the operating current and targeting smaller filament diameters.

Charge transport mechanisms in the LRS and HRS are essentially different. Transport in the LRS is associated with metal-like conductance, while in the HRS, the current through the disrupted portion of the filament is supported by a trap-assisted-tunneling (TAT) mechanism.[18] As shown in Fig. 17 (b), P-p amplitude in HRS monotonically decreases with the reduction of the filament diameter (I_{read} values reduce proportionally to the filament cross-section area). The read current was simulated at 50 mV read voltage using a TAT current model.[18,45] By using a single set of the earlier reported defect (oxygen vacancies)

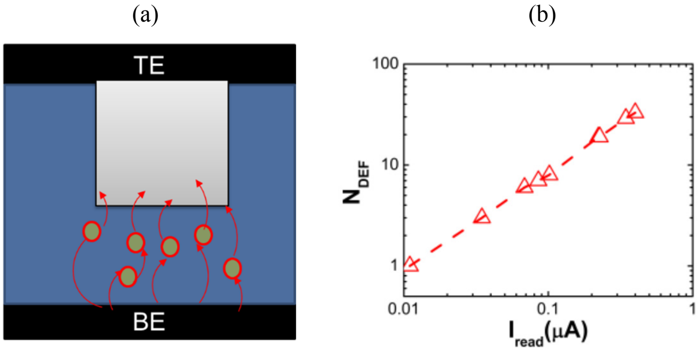

Fig. 17. (a) Schematics of TAT process in HRS: electron transport via electron capture/emission by oxygen vacancies in the oxide barrier layer. (b) TAT current simulations: Numbers of oxygen vacancies in the barrier layer, N_{DEF}, required to support the TAT current at a given measured I_{read} value (after Ref. 44).

characteristics, the HRS current was successfully reproduced in the entire range of devices with filaments of various sizes formed under different compliance current conditions, it yielded the number of traps (N_{DEF}) needed to support the corresponding read currents. To evaluate the fluctuations, it was considered that the traps supporting HRS current can be activated/deactivated by the electron capture/emission processes. Activation/deactivation of traps in the current path causes fluctuations of the read current. Calculation of the activation/deactivation rates for N traps randomly distributed throughout the oxide barrier layer in the filament was done using a multi-phonon description.[45] Activation/deactivation of any of the N traps creates $2N$ possible combinations of the I_{HRS} current levels. The probabilities, $P(s)$, of finding a system in any of $2N$ different RTN states, $s=\{1,2, ..,2N\}$ were calculated according to the probabilities of each trap being activated/deactivated. The dispersion of theoretically simulated I_{HRS} current fluctuations is then calculated as:

$$\sigma = \sqrt{\sum_s P(s)(I_{HRS}(s) - \langle I_{HRS}\rangle)^2}\,. \tag{1}$$

The dispersion is calculated for each filament size, which depends on the used current compliance value. In a smaller (narrower) filament, the number of traps supporting TAT reduces along with the area of the barrier oxide layer. This dispersion of simulated currents correlates to the experimentally measured dependency of the mean value of I_{HRS} peak-to-peak fluctuations on the read current values (proportional to filament sizes), Fig. 18. A larger number of traps contribute to TAT transport in the devices with larger filament cross-sections (i.e. formed at larger forming compliance currents).

Accordingly, a larger number of traps can be expected to create larger fluctuations in the RRAM read current. The agreement between the theory and experimental data indicate that the origin of RTN instability in RRAM HRS is indeed electron trapping at defects in the oxide barrier layer.

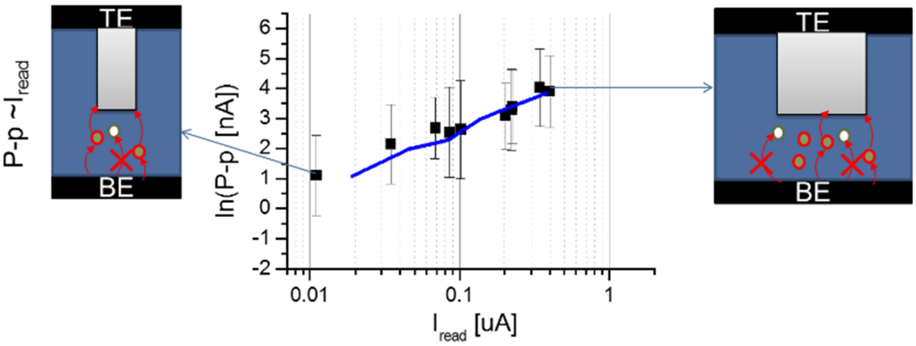

Fig. 18. The P-p amplitude of HRS read current fluctuations in the filaments of different widths (as reflected by the read current values, I_{read}, measured at a fixed voltage). The distribution of P-p amplitudes measured on each device with a filament of a certain width over multiple set/reset cycles is fitted to a log-normal distribution. Symbols show average values of P-p amplitudes extracted from the fitting performed for devices with different filament widths. Error bars represent for each device a dispersion (one σ) of the distribution of P-p amplitudes over multiple set/reset cycles, accordingly. Solid line represents a trend of the simulated P-p vs. the filament width. Insets schematically show an electron transport when activated/deactivated traps are present in narrow and wide filaments (after Ref. 44).

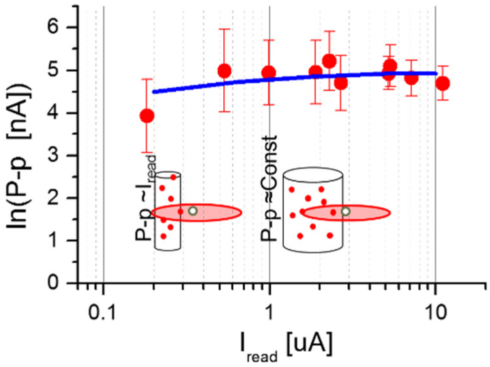

Fig. 19. Symbols: The LRS P-p amplitudes of read current fluctuations (extracted following the procedure in Fig. 16) in devices of different filament widths (resulted in different Iread values under the same selected read voltage) as formed under different current compliance conditions. Each symbol corresponds to an Iread value averaged over 200 cycles. Error bars represent the dispersion (one σ) of P-p fluctuation amplitude distribution over 200 cycles. Blue line represents the simulated dependence of the P-p fluctuation amplitude versus average read current at Vread = 50 mV, i.e., filament width. After Ref. 44.

In the LRS, the observed RTN-type of read current fluctuations can be generated by the charging/discharging of defects located in the oxide surrounding the filament (inset schematics in Fig. 19). The LRS current was modeled accounting for a partial Coulomb-blockade of the electron transport through the filament induced by these defects when they are charged by trapping injected electrons. [44] The filament section affected by the Coulomb blockade is located within a few Debye lengths from the filament interface with the surrounding oxide where the charged electron trap is located. In order to simulate the measured P-p trend, Fig. 19, RTN amplitudes for the filaments of different widths (that correspond to I_{read} values shown at the x-axis in Fig. 19) were calculated as: P-p=I_{read}- I_{read}' where I_{read} is the simulated current in the filament when the nearby oxide traps are discharged, while $I_{read'}$ is calculated accounting for the filament partially blockaded by an adjacent charged trap, by numerically solving Poisson and current continuity equations. LRS P-p amplitude noticeably decreases only in narrow filaments, (blue line in Fig. 19) when the trap effective blocking region is getting comparable to the filament cross-section. The measured amplitude dispersion gradually increases with the filament width.

Summarizing, the complex multi-level RTN-like instability observed in the LRS and HRS read currents can be evaluated using the peak-to-peak amplitude of read current fluctuations as a FoM. The parameters of FoM distributions for the set of RRAM devices operating at various read current levels can be extracted by measuring current fluctuations in a statistically significant number of set/reset cycles for each device. Using the proposed methodology, it was demonstrated that the RTN-caused read fluctuations reduce along with the operation current that removes the possible obstacle for further scaling. The mechanism for the LRS and HRS instability is the electron trapping by oxide defects in the filament vicinity.

7. Conclusion

Filament-based RRAM is demonstrated to have superior scalability, endurance, low power operation, retention, and operating speed. A challenge navigating tradeoffs between high density, low switching power and stability can be addressed by capitalizing on the developed understanding of material properties and operation conditions controlling performance of the crystalline HfO_x-based RRAM. Optimization of grain sizes and GB composition enables device scaling and their operations under extremely high frequencies and low power consumption conditions. In particular, reducing parasitics and implementing compliance-free pulsed forming and switching technique provides an effective control over the filament resistance, and hence, operation current. Read current instability, manifesting itself as a random noise observed in a read current, is found to be caused by the electron trapping/detrapping at the defect sites in the dielectric film surrounding the filament; it points to the possibilities for mitigating read instability by reducing oxygen vacancy formation during a fabrications process, as well as adjusting cell operation conditions. Further optimization of RRAM materials and operating conditions will open the path to their implementation in exascale neuromorphic computing systems.

References

1. A. Sawa, Resistive switching in transition metal oxides, *Mater. Today,* **11**, 28–36 (2008).
2. R. Waser, R. Dittmann, G. Staikov, and K. Szot, Redox-Based Resistive Switching Memories – Nanoionic Mechanisms, Prospects, and Challenges, *Adv. Mater.*, **21**, 2632–2663 (2009).
3. G. Bersuker, D. C. Gilmer, D. Veksler, J. Yum, H. Park, S. Lian, L. Vandelli, A. Padovani, L. Larcher, K. McKenna, A. Shluger, V. Iglesias, M. Porti, M. Nafria, W. Taylor, P. D. Kirsch, and R. Jammy, Metal oxide RRAM switching mechanism based on conductive filament microscopic properties, *proc. 2010 IEEE International Electron Devices Meeting (IEDM),* 19.6.1-19.6.4 (2010).

4. R. Waser and M. Aono, Nanoionics-based resistive switching memories, *Nature Materials*, **6**, 833–840 (2007).
5. B. Govoreanu, G. S. Kar, Y. Y. Chen, V. Paraschiv, S. Kubicek, A. Fantini, I. P. Radu, L. Goux, S. Clima, R. Degraeve, N. Jossart, O. Richard, T. Vandeweyer, K. Seo, P. Hendrickx, G. Pourtois, H. Bender, L. Altimime, D. J. Wouters, J. A. Kittl, and M. Jurczak, "10x10 nm^2 Hf/HfOx crossbar resistive RAM with excellent performance, reliability and low-energy operation," *in proc. 2011 IEEE International Electron Devices Meeting (IEDM)*, 31.6.1-31.6.4. (2011).
6. H. S. P. Wong H.Y. Lee, S.Yu, Metal–Oxide RRAM, *in Proceedings of the IEEE,* **100**, 1951-1970 (2012).
7. D.-H. Kwon, K. M. Kim, J. H. Jang, J. M. Jeon, M. H. Lee, G. H. Kim, X.-S Li, G.-S. Park, B. Lee, S. Han, M. Kim, C. S. Hwang, Atomic structure of conducting nanofilaments in TiO2 resistive switching memory*, Nature Nanotechnology* **5**, 148 - 153 (2010)**.**
8. Y. Y. Chen, L. Goux, S. Clima, B. Govoreanu, R. Degraeve, G. S. Kar, A. Fantini, G. Groeseneken, D. J. Wouters, and M. Jurczak, Endurance/Retention Trade-off on Cap 1T1R Bipolar RRAM*, IEEE Trans. Electron Devices*, **60**, 1114–1121 (2013).
9. P. R. Shrestha, D. Nminibapiel, J. H. Kim, J. P. Campbell, K. P. Cheung, S. Deora, G. Bersuker, and H. Baumgart, Energy control paradigm for compliance-free reliable operation of RRAM, *in proc. 2014 IEEE International Reliability Physics Symposium*, MY.10.1-MY.10.4 (2014).
10. H. Y. Lee, Y. S. Chen, P. S. Chen, P. Y. Gu, Y. Y. Hsu, S. M. Wang, W. H. Liu, C. H. Tsai, S. S. Sheu, P. C. Chiang, W. P. Lin, C. H. Lin, W. S. Chen, F. T. Chen, C. H. Lien, and M. J. Tsai, Evidence and solution of over-RESET problem for HfOx based resistive memory with sub-ns switching speed and high endurance, *in proc. 2010 IEEE International Electron Devices Meeting (IEDM)* 19.7.1-19.7.4 (2010).
11. A. C. Torrezan, J. P. Strachan, G. Medeiros-Ribeiro, and R. S. Williams, Sub-nanosecond switching of a tantalum oxide memristor, *Nanotechnology*, 22, 485203 (2011).
12. B. Cho, S. Song, Y. Ji, T.-W. Kim, T. Lee, Organic Resistive Memory Devices: Performance Enhancement, Integration, and Advanced Architectures. *Adv. Funct. Mater.*, **21**, 2806–2829 (2011).
13. Y. Hayakawa, A. Himeno, R. Yasuhara, W. Boullart, E. Vecchio, T. Vandeweyer, T. Witters, D. Crotti, M. Jurczak, S. Fujii, S. Ito, Y. Kawashima, Y. Ikeda, A. Kawahara, K. Kawai, Z. Wei, S. Muraoka, K. Shimakawa, T. Mikawa, and S. Yoneda, Highly reliable TaO_x ReRAM with centralized filament for 28-nm embedded application, *in proc. 2015 Symposium on VLSI Technology (VLSI Technology)*, T14–T15 (2015).
14. W. Wong "Non-Volatile NRAM Nanotubes Deliver Endurance and Performance" *Electronic Design*. June 3, (2015). Available online: http://electronicdesign.com/memory/non-volatile-nram-nanotubes-deliver-endurance-and-performance.
15. F. M. Puglisi, L. Larcher, G. Bersuker, A. Padovani, and P. Pavan, "An Empirical Model for RRAM Resistance in Low- and High-Resistance States," *IEEE Electron Device Lett.*, **34**, 387–389 (2013).
16. R. Degraeve, A. Fantini, S. Clima, B. Govoreanu, L. Goux, Y. Y. Chen, D. J. Wouters, P. Roussel, G. S. Kar, G. Pourtois, S. Cosemans, J. A. Kittl, G. Groeseneken, M. Jurczak, and L. Altimime, Dynamichour glass model for SET and RESET in HfO_2 RRAM, *in proc. 2012 Symposium on VLSI Technology (VLSIT)*, 75–76 (2012).
17. L. Larcher, F. M. Puglisi, P. Pavan, A. Padovani, L. Vandelli, and G. Bersuker, "A Compact Model of Program Window in HfOx RRAM Devices for Conductive Filament Characteristics Analysis," *IEEE Trans. Electron Devices*, **61**, 2668–2673 (2014).
18. L. Vandelli, A. Padovani, L. Larcher, G. Broglia, G. Ori, M. Montorsi, G. Bersuker, and P. Pavan, Comprehensive physical modeling of forming and switching operations in HfO2 RRAM

devices, *in proc. 2011 IEEE International Electron Devices Meeting (IEDM),* 17.5.1-17.5.4. (2011).

19. K. H. Xue, B. Traore, P. Blaise, L. R. C. Fonseca, E. Vianello, G. Molas, B. D. Salvo, G. Ghibaudo, B. Magyari-Kope, and Y. Nishi, A Combined Ab Initio and Experimental Study on the Nature of Conductive Filaments in Resistive Random Access Memory, *IEEE Trans. Electron Devices*, **61**, 1394–1402 (2014).
20. B. Magyari-Kope, L. Zhao, K. Kamiya, M. Y. Yang, M. Niwa, K. Shiraishi, and Y. Nishi, The Interplay between Electronic and Ionic Transport in the Resistive Switching Process of Random Access Memory Devices, *ECS Trans.*, **64**, 153–158 (2014).
21. B. Butcher, G. Bersuker, D. C. Gilmer, L. Larcher, A. Padovani, L. Vandelli, R. Geer, and P. D. Kirsch, Connecting the physical and electrical properties of Hafnia-based RRAM, *in proc. 2013 IEEE International Electron Devices Meeting*, 22.2.1-22.2.4 (2013).
22. J. Lee, J. Shin, D. Lee, W. Lee, S. Jung, M. Jo, J. Park, K. P. Biju, S. Kim, S. Park, and H. Hwang, Diode-less nano-scale ZrOx/HfOx RRAM device with excellent switching uniformity and reliability for high-density cross-point memory applications, *in proc. 2010 IEEE International Electron Devices Meeting (IEDM)*, 19.5.1-19.5.4. (2010).
23. H. Y. Lee, P. S. Chen, T. Y. Wu, Y. S. Chen, C. C. Wang, P. J. Tzeng, C. H. Lin, F. Chen, C. H. Lien, and M. J. Tsai, Low power and high speed bipolar switching with a thin reactive Ti buffer layer in robust HfO2 based RRAM, *in proc. 2008 IEEE International Electron Devices Meeting,* 1–4 (2008).
24. D. Nminibapiel, D. Veksler, P.R. Shrestha, J.P. Campbell, J-H. Kim, J.C. Ryan, H. Baumgart, K.P. Cheung, The Failure of RRAM Program-Verify; a Second Look. *2016 IEEE International Electron Devices Meeting (IEDM)*, submitted.
25. A. Belmonte, A. Fantini, A. Redolfi, M. Houssa, M. Jurczak, and L. Goux, Excellent Roff/Ron ratio and short programming time in Cu/Al2O3-based conductive-bridging RAM under low-current (10□µA) operation, *Phys. Status Solidi A*, **213**, 302–305 (2016).
26. M. Kund, G. Beitel, C. U. Pinnow, T. Rohr, J. Schumann, R. Symanczyk, K. Ufert, and G. Muller, Conductive bridging RAM (CBRAM): an emerging non-volatile memory technology scalable to sub 20nm, *in proc IEEE 2005 International Electron Devices Meeting. IEDM Technical Digest.*, 754–757 (2005).
27. A. Thomas, Memristor-based neural networks, *J. Phys. Appl. Phys.*, **46**, 93001 (2013).
28. M. D. Pickett, G. Medeiros-Ribeiro, and R. S. Williams, A scalable neuristor built with Mott memristors, *Nature Mater.*, **12**, 114–117 (2013).
29. M. Prezioso, I. Kataeva, F. Merrikh-Bayat, B. Hoskins, G. Adam, T. Sota, K. Likharev, and D. Strukov, Modeling and implementation of firing-rate neuromorphic-network classifiers with bilayer Pt/Al2O3/TiO2x/Pt Memristors, *in proc 2015 IEEE International Electron Devices Meeting (IEDM)*, 17.4.1-17.4.4. (2015).
30. M. Prezioso, F. Merrikh-Bayat, B. D. Hoskins, G. C. Adam, K. K. Likharev, and D. B. Strukov, Training and operation of an integrated neuromorphic network based on metal-oxide memristors, *Nature*, **521**, 61–64 (2015).
31. K. McKenna and A. Shluger, The interaction of oxygen vacancies with grain boundaries in monoclinic HfO_2, *Appl. Phys. Lett.*, **95**, 222111 (2009).
32. K. P. McKenna and A. L. Shluger, Electronic properties of defects in polycrystalline dielectric materials, *Microelectron. Eng.*, **86**, 1751–1755 (2009).
33. A. Padovani, L. Larcher, O. Pirrotta, L. Vandelli, and G. Bersuker, Microscopic Modeling of HfOx RRAM Operations: From Forming to Switching, *IEEE Trans. Electron Devices*, **62**, 1998–2006 (2015).
34. M. Lanza, K. Zhang, M. Porti, M. Nafría, Z. Y. Shen, L. F. Liu, J. F. Kang, D. Gilmer, and G. Bersuker, Grain boundaries as preferential sites for resistive switching in the HfO_2 resistive random access memory structures, *Appl. Phys. Lett.,* **100**, 123508 (2012).

35. G. Bersuker and D. C. Gilmer, Metal oxide resistive random access memory (RRAM) technology, *in Advances in Non-volatile Memory and Storage Technology*. Edited by Yoshio Nishi. ISBN 9780857098030. 288-340 (2014)
36. S. Deora, G. Bersuker, K. Matthews, D. C. Gilmer, and P. D. Kirsch, AC Variability and Endurance Measurement Technique for Resistive Switching Memories, *IEEE Trans. Device Mater. Reliab.*,**14**, 300–303 (2014).
37. H. Y. Chen, S. Yu, B. Gao, P. Huang, J. Kang, and H. S. P. Wong, HfOx based vertical resistive random access memory for cost-effective 3D cross-point architecture without cell selector, *in proc 2012 IEEE International Electron Devices Meeting (IEDM)*, 20.7.1-20.7.4 (2012).
38. A. Kalantarian, G. Bersuker, D. C. Gilmer, D. Veksler, B. Butcher, A. Padovani, O. Pirrotta, L. Larcher, R. Geer, Y. Nishi, and P. Kirsch, Controlling uniformity of RRAM characteristics through the forming process, *in proc 2012 IEEE International Reliability Physics Symposium (IRPS)*, 6C.4.1-6C.4.5 (2012).
39. A. Ghetti, C. M. Compagnoni, F. Biancardi, A. L. Lacaita, S. Beltrami, L. Chiavarone, A. S. Spinelli, and A. Visconti, Scaling trends for random telegraph noise in deca-nanometer Flash memories, *in proc 2008 IEEE International Electron Devices Meeting (IEDM)*, 1–4 (2008).
40. G. Ghibaudo, T. Boutchacha, Electrical noise and RTS fluctuations in advanced CMOS devices. *Microelectronics Reliability*, **42**, 573–582 (2002).
41. D. Ielmini, F. Nardi, and C. Cagli, Resistance-dependent amplitude of random telegraph-signal noise in resistive switching memories, *Appl. Phys. Lett.*, **96**, 53503 (2010).
42. R. Soni, P. Meuffels, A. Petraru, M. Weides, C. Kügeler, R. Waser, and H. Kohlstedt, Probing Cu doped Ge0.3Se0.7 based resistance switching memory devices with random telegraph noise, *J. Appl. Phys.*, **107**, 24517 (2010).
43. D. Veksler, G. Bersuker, B. Chakrabarti, E. Vogel, S. Deora, K. Matthews, D. C. Gilmer, H. F. Li, S. Gausepohl, and P. D. Kirsch, Methodology for the statistical evaluation of the effect of random telegraph noise (RTN) on RRAM characteristics, *in proc 2012 IEEE International Electron Devices Meeting (IEDM)*, 9.6.1-9.6.4 (2012).
44. D. Veksler, G. Bersuker, L. Vandelli, A. Padovani, L. Larcher, A. Muraviev, B. Chakrabarti, E. Vogel, D. C. Gilmer, and P. D. Kirsch, Random telegraph noise (RTN) in scaled RRAM devices, *in proc 2013 IEEE International Reliability Physics Symposium (IRPS),* MY.10.1-MY.10.4 (2013).
45. L. Vandelli, A. Padovani, L. Larcher, R. G. Southwick, W. B. Knowlton, and G. Bersuker, A Physical Model of the Temperature Dependence of the Current Through Stacks, *IEEE Trans. Electron Devices,* **58**, 2878–2887 (2011).